INTERNATIONAL JOURNAL FOR NUMERICAL METHODS IN FLUIDS
Int. J. Numer. Meth. Fluids 2009; **59**:907–925
Published online 19 June 2008 in Wiley InterScience (www.interscience.wiley.com). DOI: 10.1002/fld.1851

Linear and non-linear simulations of feedback control in plane Poiseuille flow

J. McKernan[1], G. Papadakis[1,*,†] and J. F. Whidborne[2]

[1]*Department of Mechanical Engineering, King's College London, Strand, London WC2R 2LS, U.K.*
[2]*Department of Aerospace Sciences, Cranfield University, Bedfordshire MK43 0AL, U.K.*

SUMMARY

This paper examines the performance of optimal linear quadratic state and output feedback controllers in stabilizing two-dimensional perturbations in a plane Poiseuille flow. The synthesis of the controllers is based on a linearized model of the flow using a new set of interpolating polynomials in the wall-normal direction, which automatically satisfy the homogeneous Dirichlet and Neumann boundary conditions at the walls and eliminate spurious eigenvalues. The controllers are implemented into a non-linear Navier–Stokes solver, which is modified to compute the evolution of the flow perturbations. Two cases are examined, one with small initial disturbances that do not violate the linearity assumptions and the other with much larger disturbances that trigger the non-linear convection terms. For the smallest disturbances, the solver accurately reproduced the results of the linear simulations of open- and closed-loop systems. The simulations for the larger disturbances without control showed a rapid initial growth but the flow soon reached a saturated state in agreement with previous findings in the literature. The large initial growth is a consequence of the non-normal nature of the system dynamics. The state feedback and output feedback controllers were able to reduce significantly the perturbation energy. For the larger disturbances, the energy calculated from the state variables is well below the energy evaluated by direct integration of the velocity field. This is probably due to the non-linear terms transferring energy to harmonics of the considered wavenumber, which are not sensed by the linear controller. Copyright © 2008 John Wiley & Sons, Ltd.

Received 21 September 2007; Revised 18 April 2008; Accepted 21 April 2008

KEY WORDS: stability; laminar flow; incompressible flow; Navier–Stokes equations; finite volume methods; spectral discretization

1. INTRODUCTION

It is well known that laminar and turbulent flows have entirely different characteristics. In laminar flow the velocity field is smooth, whereas in turbulent flow it fluctuates chaotically, leading to

*Correspondence to: G. Papadakis, Department of Mechanical Engineering, King's College London, Strand, London WC2R 2LS, U.K.
†E-mail: george.papadakis@kcl.ac.uk

strong mixing between adjacent fluid layers. The enhanced mixing results in large increases in fluid drag and therefore if transition to turbulence is suppressed, substantial savings in the energy required to sustain the flow can be obtained.

The process of transition begins with the rapid growth of small disturbances in laminar flow. One of the most widely studied flows in this respect is the one between parallel flat plates (also known as plane Poiseuille flow). This flow is linearly unstable for Reynolds numbers above 5772 [1]. However, experiments show that it undergoes transition to turbulence for Reynolds number as low as 1000, for example, as shown in [2]. This is due to the fact that, although the perturbed flow is linearly stable, the transient perturbation energy can reach values high enough that can trigger three-dimensional non-linearities that will eventually lead to transition and turbulence. Therefore, measures of the maximum perturbation energy are of interest. For a linearized system, the largest perturbation energy can be evaluated for all possible unit energy initial disturbances, and the maximum over all time gives the maximum transient perturbation energy [3–5].

Linear systems theory provides a very effective tool for control of non-linear problems, such as the Navier–Stokes equations, as explained in a recent review [6]. This opens the possibility of using standard modern control theory (e.g. [7, 8]) to develop controllers that can stabilize the flow. It has been shown that linearized systems do represent some important dynamic processes of turbulent flows. For example, in [9] a coupling term is identified in the linearized Navier–Stokes equations without which near wall turbulence is shown to decay (other references are provided in [6]). There are various ways of sensing the state of the flow (for example, through measurement of shear stresses or pressure) and influencing the flow (for example, through suction and blowing at the walls). Linear models are often based on spectral analysis of the linearized equations as performed, for example, in [4, 10, 11].

In this context, the purpose of the present paper is to examine the performance of optimal linear quadratic state and output feedback controllers in stabilizing two-dimensional perturbations in a plane Poiseuille flow. The state-space model assumes streamwise periodicity at a single wavenumber in flow, measurement and control variables, and employs a novel polynomial wall-normal basis that produces a system free of spurious eigenmodes and leads to control via the rate of change of wall-normal transpiration velocity. In addition, the synthesized controllers are subsequently tested in a full model of the flow using a non-linear Navier–Stokes solver, which is completely independent of the development model. The performance of the linearly designed controllers is also examined for finite-amplitude perturbations that trigger non-linearities. In order to keep the simulation times relatively small, the flow examined is two dimensional.

A few other investigators have examined the state of the flow between parallel plates when initially infinitesimally small perturbations grow and trigger the non-linear convection terms. Two-dimensional simulations are reported in [12] that extend the linear stability curve to neutral finite-amplitude states. The authors found that for a Reynolds number below 2827 any single mode disturbance to the parabolic profile in the streamwise direction dies away. For Reynolds number and wavenumbers for which the linear theory predicts instability, an initial disturbance of any amplitude eventually saturates to a single finite-amplitude solution. For Reynolds greater than 2827, but outside the linear instability region, a ‘subcritical instability’ with two steady solution branches occurs for wavenumbers in a given band. The solution branch with the smallest amplitude is known to be unstable for two-dimensional disturbances, whereas the other one is, at least for moderate Reynolds numbers, not only stable but also attracting. Both branches are known to be unstable for three-dimensional perturbations [13]. More detailed two-dimensional simulations have also been performed by Jimenez [14, 15] who investigated the flow dynamics of the upper branch.

DOI: 10.1002/fld

He found that for certain combinations of Reynolds and wavenumbers the steady flow branch bifurcates into one-frequency limit cycles or two-frequency tori. Three-dimensional computations are reported in [16].

The paper is organized as follows: Section 2 briefly introduces the linear and non-linear perturbation equations and the selected formulation. It also presents the modified Chebyshev polynomials that are used for the wall-normal discretization. Section 3 describes the synthesis of optimal state feedback controllers and optimal state estimators. Section 4 details implementation issues of the controllers to a full Navier–Stokes finite volume code. Section 5 presents results from linear and non-linear simulations with smaller and larger initial disturbances, respectively, around a laminar (parabolic) velocity profile. In the simulations, the open-loop (OL) system comprises the plant model with an optimal linear quadratic estimator (LQE). The closed-loop systems comprise the plant model either with a state feedback linear quadratic regulator (LQR) or with a output feedback linear quadratic Gaussian (LQG) control. Finally the last section draws conclusions regarding the performance of controllers and estimator.

2. FLOW EQUATIONS AND STATE-SPACE REPRESENTATION

2.1. Linear and non-linear perturbation equations

The flow of an incompressible Newtonian fluid is described by the Navier–Stokes and continuity equations. This set of equations describes both a base flow ($\mathbf{U}_\mathrm{b}=(U_\mathrm{b}, V_\mathrm{b}, W_\mathrm{b})$, P_b) and any perturbed state ($(U_\mathrm{b}+u, V_\mathrm{b}+v, W_\mathrm{b}+w)$, $P_\mathrm{b}+p$) of the base flow. The evolution equations of the disturbances, which are derived by subtracting the equations of the base state from those of the perturbed state, are shown below:

$$\frac{\partial \mathbf{u}}{\partial t}+(\mathbf{u}\cdot\nabla)\mathbf{u}+\underline{(\mathbf{U}_\mathrm{b}\cdot\nabla)\mathbf{u}}+\underline{(\mathbf{u}\cdot\nabla)\mathbf{U}_\mathrm{b}}=-\frac{1}{\rho}\nabla p+\frac{\mu}{\rho}\nabla^2\mathbf{u} \tag{1}$$

$$\nabla\cdot\mathbf{u}=0 \tag{2}$$

where μ is the dynamic viscosity and ρ the density of the fluid. In order to derive a linear state-space representation of the form $\dot{\mathscr{X}}=\mathscr{A}\mathscr{X}+\mathscr{B}\mathscr{U}$ required for the application of modern control theory ($\mathscr{X}$ being the state variables and $\mathscr{U}$ the inputs), this set of equations must be linearized around the base flow. In this paper the laminar flow between parallel flat plates, with x being the streamwise direction, y the wall-normal direction and z the spanwise direction, is considered to be the base flow. In non-dimensional values the upper and lower walls are located in $y=1$ and -1, respectively, and the velocity vector is $\mathbf{U}_\mathrm{b}=(1-y^2, 0, 0)$. The channel half-height h and the centreline velocity U_cl are the reference quantities, respectively, for the non-dimensionalization.

The continuity perturbation equation is already linear. The perturbation Navier–Stokes equations can be linearized by discarding the second-order quantity $(\mathbf{u}\cdot\nabla)\mathbf{u}$, which is small compared with the underlined terms $(\mathbf{U}_\mathrm{b}\cdot\nabla)\mathbf{u}+(\mathbf{u}\cdot\nabla)\mathbf{U}_\mathrm{b}$ when $\mathbf{u}\ll\mathbf{U}_\mathrm{b}$, resulting in the following set:

$$\frac{\partial \mathbf{u}}{\partial t}+(\mathbf{U}_\mathrm{b}\cdot\nabla)\mathbf{u}+(\mathbf{u}\cdot\nabla)\mathbf{U}_\mathrm{b}=-\frac{1}{\rho}\nabla p+\frac{\mu}{\rho}\nabla^2\mathbf{u} \tag{3}$$

$$\nabla\cdot\mathbf{u}=0 \tag{4}$$

DOI: 10.1002/fld

Although the system is linear, it still cannot be used to derive a state-space model of the required form. The reason is that although the discretized form of this system can be put in the form $\mathscr{L}\dot{\mathscr{X}}=\mathscr{A}\mathscr{X}+\mathscr{B}\mathscr{U}$, matrix $\mathscr{L}$ is singular and cannot be inverted. This singularity stems from the fact that for incompressible flows pressure does not appear as an unknown variable in the continuity equation. In order to proceed, system (3), (4) must be reformulated in such a way that the continuity constraint is implicitly enforced. There are several possible formulations such as vorticity–stream function, velocity–vorticity, etc. as described in [17]. The current study employs a velocity–vorticity formulation as it is convenient for the application of boundary conditions in the examined geometry.

2.2. *Velocity–vorticity formulation*

Using the continuity equation (4), the pressure perturbation can be eliminated from the linearized equations (3) to yield an equation for the wall-normal velocity:

$$\left(\frac{\partial}{\partial t}\right)\left(\frac{\partial^2 v}{\partial x^2}+\frac{\partial^2 v}{\partial y^2}\right)+U_\mathrm{b}\left(\frac{\partial}{\partial x}\right)\left(\frac{\partial^2 v}{\partial x^2}+\frac{\partial^2 v}{\partial y^2}\right)-\frac{\partial^2 U_\mathrm{b}}{\partial y^2}\frac{\partial v}{\partial x}-\frac{1}{R}\left(\frac{\partial^4 v}{\partial x^4}+\frac{\partial^4 v}{\partial y^4}\right)=0 \tag{5}$$

where $U_\mathrm{b}=1-y^2$ and R is the Reynolds number (defined as $R=\rho U_\mathrm{cl}h/\mu$ with h being the half-height of the channel). This fourth-order partial differential equation suffices to describe the two-dimensional perturbations considered in this paper. A second equation, in vorticity, is required to completely describe a three-dimensional perturbation.

This equation is supplemented with the boundary conditions. At the walls, the velocity perturbation, $v(y=\pm 1)$, is zero and due to continuity equation, the y derivative of v is also zero. These are four boundary conditions for the fourth-order equation thus forming a well-posed mathematical problem.

A spectral method is employed for the discretization of this equation. The variation in the x direction is assumed to be periodic and is approximated by a truncated Fourier series expansion. The linearized equations decouple by wavenumber and thus it is possible to treat each number separately. Therefore for the wavenumber α we have

$$v(x,y,t)=\mathrm{Re}(\tilde{v}(y,t)\mathrm{e}^{\mathrm{i}\alpha x}) \tag{6}$$

where $\tilde{v}(y,t)$ is the Fourier coefficient of the wall-normal velocity perturbation, or simply the velocity coefficient. This is a complex number and conveys the wall-normal (y) and temporal (t) variation of v at the streamwise wavenumber α. Substituting the assumed solution (6) into Equation (5) we get

$$\left(-U_\mathrm{b}\alpha^2-\frac{\partial^2 U_\mathrm{b}}{\partial y^2}-\frac{\alpha^3}{\mathrm{i}R}\right)\tilde{v}+\left(U_\mathrm{b}+\frac{2\alpha}{\mathrm{i}R}\right)\frac{\partial^2\tilde{v}}{\partial y^2}-\left(\frac{1}{\mathrm{i}R\alpha}\right)\frac{\partial^4\tilde{v}}{\partial y^4}=\frac{\mathrm{i}}{\alpha}\left(\frac{\partial^3\tilde{v}}{\partial y^2\partial t}-\alpha^2\frac{\partial\tilde{v}}{\partial t}\right) \tag{7}$$

The boundary conditions for $\tilde{v}(y)$ are identical to those for v, i.e. the value and the first-order derivative with respect to y at the walls are both equal to 0. If an exponential time variation is assumed, the classical Orr–Sommerfeld equation is derived.

DOI: 10.1002/fld

2.3. Discretization in the wall-normal direction

In the wall-normal direction $\tilde{v}(y)$ is approximated by polynomials Ξ_n

$$\tilde{v}(y,t)=\sum_{n=1}^{N} a_n(t)\Xi_n(y) \tag{8}$$

where $a_n(t)$ are unknown spectral coefficients. Substitution of series (8) into velocity equation (7) yields a system of first-order ordinary differential equations for the spectral coefficients $a_n(t)$. The polynomials Ξ_n are usually the standard Chebyshev polynomials. This set, however, results in spurious eigenvalues as four equations next to the walls (two from the top and two from the bottom) must be discarded and replaced by algebraic ones that represent the required Dirichlet and Neumann conditions. More details about their origin in generalized eigenvalue problems in non-periodic geometries due to the misapplication of boundary conditions are provided in [18]. Inclusion of spurious eigenvalues in the system matrix $\mathscr{A}$ can cause problems when applying control theory and therefore they have to be identified and moved to highly damped areas. This can be done by a suitable choice of the algebraic coefficients [19].

In this paper, a different approach is followed. A set of modified Chebyshev polynomials that individually satisfy the Dirichlet as well as the Neumann boundary conditions at the wall is used. This guarantees that $\tilde{v}(y)$ will automatically satisfy these conditions as well and therefore no modifications are required close to the walls. The following modified Chebyshev polynomials are used as basis functions in the present paper:

$$\Xi_{n,\mathrm{odd}}=(\Gamma_{n+4}-\Gamma_1)-\frac{(n+3)^2(\Gamma_{n+2}-\Gamma_1)}{(n+1)^2} \tag{9}$$

$$\Xi_{n,\mathrm{even}}=(\Gamma_{n+4}-\Gamma_2)-\frac{((n+3)^2-1)(\Gamma_{n+2}-\Gamma_2)}{(n+1)^2-1} \tag{10}$$

where $\Gamma_n(y)$ are the standard Chebyshev polynomials. It is reminded that $\Gamma_1=1$ and $\Gamma_2=y$. It can be easily seen that since for $n>2$, $\Gamma_n(\pm1)=(\pm1)^{n-1}$ [20, p. 159] (and therefore $\Gamma_{n,\mathrm{odd}}(\pm1)=\Gamma_1(\pm1)$ and $\Gamma_{n,\mathrm{even}}(\pm1)=\Gamma_2(\pm1)$), this recombination satisfies the homogeneous Dirichlet boundary condition, i.e.

$$\Xi_n(\pm1)=0 \tag{11}$$

In addition, since $\Gamma_1'(\pm1)=0$ and $\Gamma_{n>1}'(\pm1)=(\pm1)^{n-2}(n-1)^2$ (see again [20, p. 159]), it can be easily verified upon substitution that it also satisfies the homogeneous Neumann boundary condition, i.e.

$$\Xi_n'(\pm1)=0 \tag{12}$$

This set of modified polynomials is believed to be new and to the best of the authors' knowledge has not been used before for the wall-normal discretization. They eliminate spurious eigenvalues and have good stability characteristics as shown in [21].

2.4. State-space representation

In order to derive the state-space form, Equation (8) is substituted into (7) and the resulting expression is evaluated at the Gauss–Lobatto collocation points. The state variables are simply

DOI: 10.1002/fld

the spectral coefficients a_n, which multiply the modified Chebyshev polynomials. Although this choice is less intuitive than the collocation point values, the number of spectral coefficients can be easily reduced when required due to the fast convergence of Chebyshev series.

The control variables in the present study are related to the rate of change of transpiration, i.e. the wall-normal velocity perturbation on the upper and lower walls, $\tilde{q}_u = \tilde{v}(y=1)$ and $\tilde{q}_l = \tilde{v}(y=-1)$. As these are Fourier coefficients, physically they correspond to sinusoidal streamwise distribution of transpiration velocity at the selected wavenumber. Since the distributions are sinusoidal, zero-net mass transpiration is automatically enforced. The introduction of wall transpiration makes the v velocities non-zero at the wall but a new variable can be defined and substituted whose boundary value is zero and so the polynomials presented earlier can still be used [22].

The state-space model requires fluid flow measurements, and the least intrusive at reasonable cost are those of wall shear stresses. Thus, the measurement variables in the present study are the Fourier coefficients of the wall shear stress on the upper and lower walls.

There are no numerical problems in having the sensing of shear, $1/R\partial u/\partial y$, and actuation, by setting $\partial v/\partial t$, collocated on the walls. The actuation affects the measurement via the system dynamics, which are derived from the Navier–Stokes and continuity equations. Physical collocation is of course not possible but might be approximated by the use of micro-electronic devices.

Further details on the introduction of wall transpiration, the expression of the wall shear stress in terms of the state variables and the final expression of the state-space form are provided in [21, 22]. The synthesis of the controllers for this linear system is presented in the following section.

3. CONTROLLER SYNTHESIS

3.1. Optimal state feedback

The standard LQR control problem states that given the open loop (OL) system or 'plant'

$$\begin{aligned} \dot{\mathscr{X}} &= \mathscr{A}\mathscr{X} + \mathscr{B}\mathscr{U} \\ \mathscr{Y} &= \mathscr{C}\mathscr{X} \end{aligned} \tag{13}$$

where $\mathscr{Y}$ are the outputs (in the present case the measurements of the wall shear stress), the feedback control signal that minimizes the functional

$$\int_0^\infty (\mathscr{X}(t)^{\mathrm{T}} \mathscr{Q} \mathscr{X}(t) + \mathscr{U}(t)^{\mathrm{T}} \mathscr{R} \mathscr{U}(t))\, \mathrm{d}t \tag{14}$$

where $\mathscr{Q} = \mathscr{Q}^{\mathrm{T}} \geqslant 0$ and $\mathscr{R} = \mathscr{R}^{\mathrm{T}} > 0$ are weighting matrices, is given by $\mathscr{U} = -\mathscr{K}\mathscr{X}$ where $\mathscr{K} = \mathscr{R}^{-1}\mathscr{B}^{\mathrm{T}}\mathscr{P}$ and $\mathscr{P} = \mathscr{P}^{\mathrm{T}} \geqslant 0$ is the solution of the algebraic Riccati equation

$$\mathscr{A}^{\mathrm{T}}\mathscr{P} + \mathscr{P}\mathscr{A} - \mathscr{P}\mathscr{B}\mathscr{R}^{-1}\mathscr{B}^{\mathrm{T}}\mathscr{P} + \mathscr{Q} = 0 \tag{15}$$

Figure 1 shows a block diagram of LQR state feedback. A natural choice for matrix $\mathscr{Q}$ is such that $\mathscr{X}^{\mathrm{T}}\mathscr{Q}\mathscr{X}$ equals the transient energy density E (i.e. energy per unit volume), defined as

$$E = \frac{1}{V}\int_V \rho \frac{\mathbf{u}^{\mathrm{T}}\mathbf{u}}{2}\, \mathrm{dvol} \tag{16}$$

DOI: 10.1002/fld

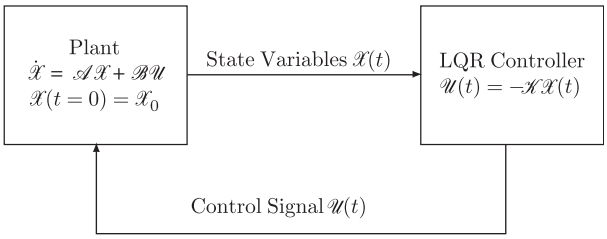

Figure 1. A block diagram of LQR state feedback.

where **u** is the perturbation velocity vector. The analytic expressions for the elements of matrix $\mathscr{Q}$ are provided in [21].

Matrix $\mathscr{R}$ is set as $\mathscr{R} = r^2\mathbf{I}$, where **I** is the identity matrix. In practice, r quantifies the 'price' of the control. A large value of r results in small values of the control variables (i.e. 'expensive' control), whereas small values tend to result in larger control magnitude and smaller transient energy density (see [23] for more details). A value of $r = 0.25$ is selected for all the calculations.

3.2. Optimal estimation

The standard LQE problem assumes that the system has disturbance and measurement noise input processes w_d and w_n, respectively,

$$\begin{aligned} \dot{\mathscr{X}} &= \mathscr{A}\mathscr{X} + \mathscr{B}\mathscr{U} + w_\mathrm{d} \\ \mathscr{Y} &= \mathscr{C}\mathscr{X} + w_\mathrm{n} \end{aligned} \tag{17}$$

and that the noise inputs are uncorrelated, zero-mean, Gaussian stochastic processes with constant power spectral density matrices $\mathscr{V}$ and $\mathscr{W}$ [8, p. 353]. The theory states that for an LQE state estimator

$$\dot{\hat{\mathscr{X}}} = \mathscr{A}\hat{\mathscr{X}} + \mathscr{B}\mathscr{U} + \mathscr{L}(\mathscr{Y} - \mathscr{C}\hat{\mathscr{X}}) \tag{18}$$

where $\hat{\mathscr{X}}$ are the estimated state variables, the optimal estimator gain $\mathscr{L}$ that minimizes

$$\mathrm{Exp}\{[\hat{\mathscr{X}} - \mathscr{X}]^\mathrm{T}[\hat{\mathscr{X}} - \mathscr{X}]\} \tag{19}$$

(Exp being the expectation operator) is given by $\mathscr{L} = \mathscr{P}\mathscr{C}^\mathrm{T}\mathscr{V}^{-1}$ where $\mathscr{P} = \mathscr{P}^\mathrm{T} \geqslant 0$ is the solution of the algebraic Riccati equation

$$\mathscr{P}\mathscr{A}^\mathrm{T} + \mathscr{A}\mathscr{P} - \mathscr{P}\mathscr{C}^\mathrm{T}\mathscr{V}^{-1}\mathscr{C}\mathscr{P} + \mathscr{W} = 0 \tag{20}$$

This equation is solved using the MATLAB Robust Control Toolbox `aresolv` function. The statistical properties of the noise inputs on the present system are unknown, and matrices $\mathscr{V}$ and $\mathscr{W}$ can be treated as parameters that can be tuned in order to achieve an estimator of acceptable performance. Details about the selection of the $\mathscr{V}$ and $\mathscr{W}$ are provided in [23].

DOI: 10.1002/fld

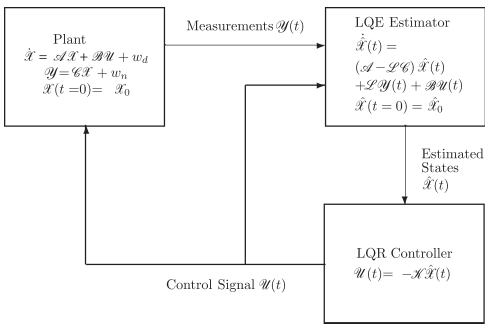

Figure 2. A block diagram of LQG output feedback.

3.3. Optimal output feedback

The combined plant, LQR controller and LQE estimator may be combined into an LQG output feedback system, with dynamics

$$\begin{bmatrix} \dot{\mathscr{X}} \\ \dot{\hat{\mathscr{X}}} \end{bmatrix} = \begin{bmatrix} \mathscr{A} & -\mathscr{B}\mathscr{K} \\ \mathscr{L}\mathscr{C} & \mathscr{A} - \mathscr{B}\mathscr{K} - \mathscr{L}\mathscr{C} \end{bmatrix} \begin{bmatrix} \mathscr{X} \\ \hat{\mathscr{X}} \end{bmatrix} + \begin{bmatrix} \mathbf{I} & \mathbf{0} \\ \mathbf{0} & \mathscr{L} \end{bmatrix} \begin{bmatrix} \omega_\mathrm{d} \\ \omega_\mathrm{n} \end{bmatrix} \tag{21}$$

where the estimate and state dynamics are not independent but are intentionally coupled. Figure 2 shows a block diagram of LQG output feedback.

The state-space model is coded in MATLAB. Detailed linear simulations are performed for the OL, state feedback and output feedback systems, from the worst initial conditions, using the MATLAB function `lsim`. These conditions are calculated as described in [4] following [3]. Non-linear simulations are performed using a Navier–Stokes solver, which is appropriately modified as explained in the following section.

4. IMPLEMENTATION TO A NON-LINEAR NAVIER–STOKES SOLVER

4.1. Solution of the non-linear perturbation equations

The code in which the aforementioned controllers are implemented solves the full non-linear Navier–Stokes equations using the finite volume discretization method and it is completely independent of the MATLAB spectral code used for the controller synthesis and linear simulations. The solver employs an unstructured, collocated grid capable of representing complex geometries. A second-order central differencing scheme is used to discretize the spatial terms and a second-order Euler 3-point implicit scheme is used for time marching. The PISO algorithm is used to handle pressure–velocity coupling.

Early simulations showed that if the algorithm solves for the total velocity components, i.e. $\mathbf{U} = \mathbf{U}_\mathrm{b} + \mathbf{u}$, then excessively fine meshes are required in order to get close agreement between the linear and non-linear results for very small perturbations. The origin of this discrepancy was

DOI: 10.1002/fld

traced to the discretization errors that contaminate the numerical solution of the base flow $\mathbf{U}_b$. These errors can be of the same order of magnitude as $\mathbf{u}$ and must be minimized in order to be able to study the evolution of the perturbations, thus the need for very fine meshes.

In order to solve the problem, the existing CFD code is modified to solve the system of the non-linear perturbation equations (1), (2), which contain exactly the same information as the standard Navier–Stokes equations. For the base flow velocity that appears explicitly the analytic solution $\mathbf{U}_b = (1-y^2, 0, 0)$ is directly employed. The difference between the standard and the perturbation Navier–Stokes equations are the two underlined terms in (1). The first term $(\mathbf{U}_b \cdot \nabla)\mathbf{u}$ is treated as a convection term, i.e. the velocity $\mathbf{U}_b$ is added directly to convection velocities at the faces of each control volume, whereas the second term $(\mathbf{u} \cdot \nabla)\mathbf{U}_b$ is moved to the right-hand side and is treated as a source term. The continuity equations for the total velocities $\mathbf{U}$ and for perturbation velocities $\mathbf{u}$ are identical; hence, no modification was necessary. Clearly from the solution of this set of partial differential equations, the perturbation velocity and pressure fields are obtained.

The boundary conditions are cyclic with constant mass flow rate in the streamwise direction and symmetric in the spanwise direction. The streamwise cyclic boundary conditions and domain length $2\pi/\alpha$ enforce periodic flow behaviour at wavenumber α. The standard wall boundary conditions are modified to simulate wall transpiration by imposing the wall-normal velocity calculated by the controller. In order to keep the mass flow rate constant a special pressure correction procedure is implemented. This constant flow rate and associated momentum are used for the normalization of the residuals of the discretized equations.

The meshes employed are structured and nominally two dimensional, the third dimension being only one cell thick, and they are generated by a short Fortran program. One of the meshes employed is shown in Figure 3. It covers one streamwise period, $x = 0 - 2\pi$, with $2^7 = 128$ uniform cells, an appropriate number for fast Fourier transform and contains 100 cells in the y (wall-normal) direction. The y coordinates of the cell centroids coincide with the Gauss–Lobatto points, thus

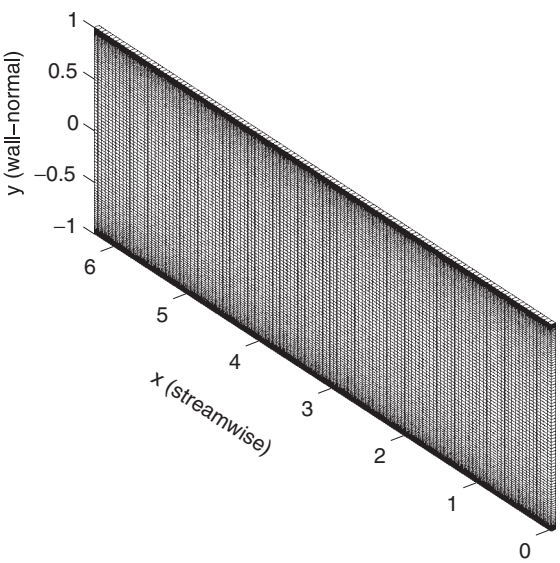

Figure 3. Isometric view of one of the finite volume meshes.

DOI: 10.1002/fld

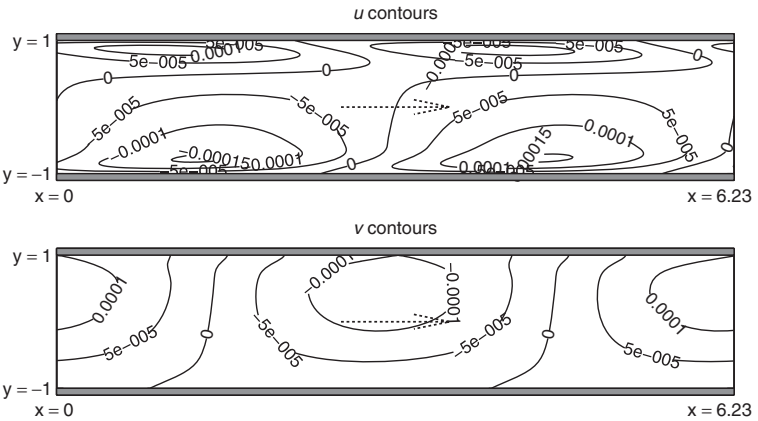

Figure 4. Contours of u and v perturbation velocities for sinusoidal upper wall transpiration of amplitude $v_{\max} = 10^{-4} U_{\mathrm{cl}} (R = 500)$. Linear (dashed line) and non-linear (solid line) results are identical.

producing cell refinement in the near wall region, and also avoiding the need for interpolation onto the location of the state variables.

The worst initial conditions (see Section 5.2) calculated from the spectral (MATLAB) code are assigned to the cell centroids and boundary faces.

The solution of the non-linear perturbation equations requires significantly more computing time than the linear simulations, in the order of days rather than minutes on a Pentium 4$^{\mathrm{TM}}$ personal computer. All calculations are in double precision.

The modified code is validated first for a steady case with imposed constant flow transpiration. Figure 4 displays the steady u and v perturbation contours from linear and non-linear simulations for a prescribed sinusoidal transpiration from the upper wall with amplitude $10^{-4} U_{\mathrm{cl}}$, where U_{cl} is the centreline velocity. The base flow corresponds to Reynolds number of 500 and the mesh used is the one shown in Figure 3. The perturbations are solely due to the imposed small amplitude transpiration. The linear solution corresponds to the eigenvector of the zero eigenvalue that represents the control actuation at the upper wall, transformed from Fourier space to physical space. It can be seen that the linear and non-linear results are indistinguishable for both u and v flow fields. Thus, it can be concluded that the boundary conditions have been implemented correctly into the CFD code and that the code and mesh are capable of accurately modelling perturbations small enough to be linear.

4.2. Incorporation of the controller into the solver

The controllers described earlier are incorporated in the aforementioned modified Navier–Stokes code. The controller matrix $\mathscr{K}$, estimator matrices $\mathscr{A}, \mathscr{B}, \mathscr{C}, \mathscr{L}$ and the matrices necessary for calculating the state variables and energy density from the flow field were evaluated using MATLAB and then imported into the code.

At each time step the code provides a perturbation velocity field. The measured wall shears, $1/R(\partial u/\partial y)$, are calculated using a first-order finite difference approximation, which is accurate enough as the collocation points are very closely spaced at the walls. Fast Fourier transforms are then performed in the streamwise direction on the velocity flow fields as well as wall shears.

DOI: 10.1002/fld

Pairs of transforms are performed simultaneously using the subroutine TWOFFT from [24, p. 398] and the Fourier coefficients $\tilde{v}(y_k)$ at the streamwise wavenumber α are selected from the results. The measurement vector is also composed from the results of fast Fourier transforms on the wall shear stresses.

For state feedback (LQR) the state variables $\mathscr{X}$ are then calculated from $\tilde{v}(y_k)$ and from these the transient energy $E = \mathscr{X}^{\mathrm{T}} \mathscr{Q} \mathscr{X}$. Estimated state variables $\hat{\mathscr{X}}$ are calculated from the measurement vector $\tilde{\mathbf{y}}$, and control vector $\mathscr{U}$ by integrating (18) using an implicit method [24, p. 575]. The initial estimated state variables $\hat{\mathscr{X}}(t=0)$ are set equal to 0.

For state feedback the control signals $\tilde{v}_u, \tilde{v}_l$ are calculated as $\mathscr{U} = -\mathscr{K} \mathscr{X}$, whereas for output feedback they are calculated as $\mathscr{U} = -\mathscr{K} \hat{\mathscr{X}}$. The control signals are integrated to yield $\tilde{v}_u, \tilde{v}_l$ using the initial conditions $\tilde{v}_u(0)$ and $\tilde{v}_l(0)$, and the wall transpiration velocities v_u, v_l are evaluated as

$$\begin{aligned} v_u(x) &= \Re(\tilde{v}_u \mathrm{e}^{\mathrm{i}\alpha x}) \\ v_l(x) &= \Re(\tilde{v}_l \mathrm{e}^{\mathrm{i}\alpha x}) \end{aligned} \tag{22}$$

for the duration of the time step.

5. RESULTS AND DISCUSSION

5.1. The case examined and discretization of the spectral model

The case considered here is two dimensional. The Reynolds number ($R = \rho U_{\mathrm{cl}} h/\mu$) is 10^4 and the streamwise wavenumber $\alpha = 1$. Accurate eigenvalues for this case are reported in [1]. One of the eigenvalues is unstable ($0.00373967 - 0.23752649\mathrm{i}$) and is known as a Tollmien–Schlichting wave [19]. Since there is no spanwise variation it is assumed that the w velocity is zero.

Before moving onto the results, it is appropriate first to consider the level of discretization of the spectral model that is used for the controller synthesis. For the LQR controller synthesis to converge a value of $N = 30$ in Equation (8) is sufficient but the LQE estimator synthesis is more exacting. For the wall gradients and observability to converge for the first 20 modes $N = 100$ is required. Thus, the major factor in determining the discretization to be used appears to be the accuracy of the wall gradients in the estimator model of the plant. Accordingly, controllers synthesized with $N = 100$ are used within the linear and non-linear simulations. Numerical tests have demonstrated that for $N = 100$ the spectral model can also achieve the high level of accuracy of eigenvalues reported in the fluid dynamics literature [1].

5.2. Comparison between linear and non-linear simulations for very small initial disturbances

The OL case examined is linearly unstable because there is one unstable eigenvalue, i.e. the transient energy is expected to rise indefinitely when the linear equations are solved. However, the rate of rise (at least at the initial stages) depends on the combined effect of the different eigenmodes. In the present paper, the initial distribution of u and v velocities consists of different eigenmodes and the contribution of each eigenmode is evaluated so that the transient energy is maximized at time 700. The calculated value of transient energy E at $t = 700$ is 5396.0 from an initial unit energy. These initial conditions are found not to vary with the precise time at which E is maximized.

DOI: 10.1002/fld

In order to assess whether the initial perturbations can be expected to behave linearly, the magnitude of the non-linear terms $(\mathbf{u}\cdot\nabla)\mathbf{u}$ omitted during the linearization process is calculated for the worst initial conditions that correspond to a maximum v amplitude of $10^{-4}U_{\mathrm{cl}}$. The non-linearity in the y momentum equation quantified by the ratio $(\mathbf{u}\cdot\nabla v)/(\mathbf{U}_{\mathrm{b}}\cdot\nabla v)$ for OL (i.e. uncontrolled case) is presented in Figure 5. The regions where this ratio is larger than 10^{-2} are confined near the walls and in total are less than 10% of the whole channel area. The plot contours scale directly with perturbation; hence for a $10^{-2}U_{\mathrm{cl}}$ perturbation, the regions with the same degree of non-linearity would cover around 45% of the area. The results for x momentum are similar. Thus, it would appear that a $10^{-4}U_{\mathrm{cl}}$ initial perturbation would produce significantly more linear behaviour than a $10^{-2}U_{\mathrm{cl}}$ one. A $10^{-4}U_{\mathrm{cl}}$ perturbation has initial transient energy of 8.23×10^{-8}, hereafter denoted by E_{linear}. The base flow energy density is $\frac{4}{15}\approx0.2667$; thus, E_{linear} has approximately 3.1×10^{-7} of the base flow energy density.

The OL transient energy from this small initial perturbation, for both linear (dotted) and non-linear (solid) simulations, is exhibited in Figure 6. The results from the linear and non-linear simulations agree very well, as might be expected from the initial small degree of non-linearity. The energy increases swiftly at a rate determined by the combined effect of the different eigenmodes that constitute the worst initial conditions (this is called non-normal growth). When all the stable

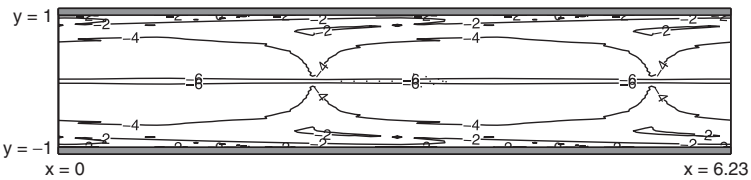

Figure 5. Contours of the ratio $\log_{10}|(\mathbf{u}\cdot\nabla v)/(\mathbf{U}_{\mathrm{b}}\cdot\nabla v)|$ for the y-momentum equation and worst initial perturbation of amplitude $v_{\max}=10^{-4}U_{\mathrm{cl}}$.

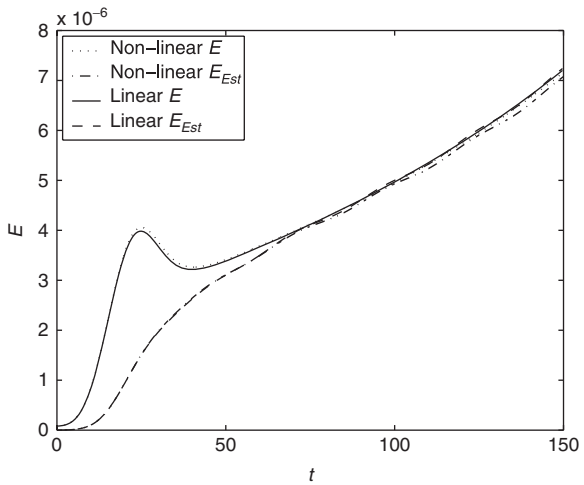

Figure 6. Open-loop transient energy E vs time t (initial conditions scaled to energy E_{linear}).

DOI: 10.1002/fld

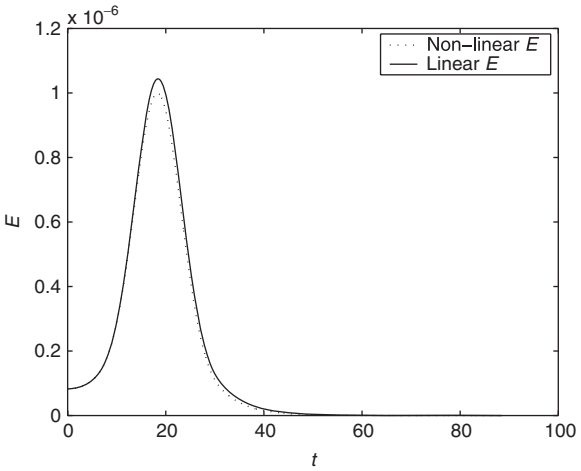

Figure 7. LQR transient energy E vs time t (initial conditions scaled to energy E_{linear}).

eigenmodes have decayed, the non-normal growth is completed and the energy continues to rise at the slower rate of a single unsteady eigenmode (normal growth). The same figure also shows the behaviour of the estimator. For good performance the estimated energy must converge with the plant energy quickly. It can be seen that the estimator cannot capture accurately the initial rapid non-normal growth but once the slower rate of the unstable eigenvalue is established, the estimator can capture the correct energy levels quite accurately.

Figure 7 presents the closed-loop LQR state feedback transient energy, from worst initial perturbations of equal energy to OL case, for both linear (solid) and non-linear (dotted) simulations. The results from both simulations again agree well (although there is a small difference at the peak) and show the stabilization (relaminarization) of the flow by the LQR controller.

It was mentioned in Section 4.2 that the energy of the system E in the non-linear simulations was evaluated from the states, i.e. $E = \mathscr{X}^{\mathrm{T}} \mathscr{Q} \mathscr{X}$. The energy thus computed agrees with the energy evaluated by direct integration of the velocity field over the mesh (16) to within 0.3%. This shows that the calculation of the state variables is correct and that the energy matrix $\mathscr{Q}$ is correctly formulated.

The behaviour of the combined LQE estimator and state feedback LQR controller on the plant from worst initial conditions of energy E_{linear} is shown in Figure 8. The non-linear simulation energy estimates again agree well with the linear simulation for both the plant and estimator transient energy. It is interesting to see that both the linear and non-linear simulations show that the estimated energy amounts to only a small fraction of the plant energy evaluated from state variables. Nonetheless the controller is able to stabilize the flow although it results in a larger energy peak compared to the LQR state feedback controller.

5.3. Comparison between linear and non-linear simulations for larger initial disturbances

Larger perturbations which trigger non-linearities are more difficult to simulate accurately. Accordingly a mesh and time step sensitivity study is performed to assess the appropriate level of discretization. The study is performed only for an OL simulation which is more demanding, since closed-loop simulations have lower peak energy levels.

DOI: 10.1002/fld

The initial conditions are the worst for the open loop eigensystem, with energy corresponding to that of a $v_{\max} = 10^{-2} U_{\mathrm{cl}}$ OL worst initial perturbation. This energy is 4 orders of magnitude larger than E_{linear} i.e. $10^4 E_{\mathrm{linear}} = 0.00082$ (approximately 3.1×10^{-3} of the base flow energy density).

Figure 9 shows the u velocity component at 4 monitoring points at 25% channel height intervals. Two meshes were examined, with N = 100 and with 150 cells in the wall-normal direction.

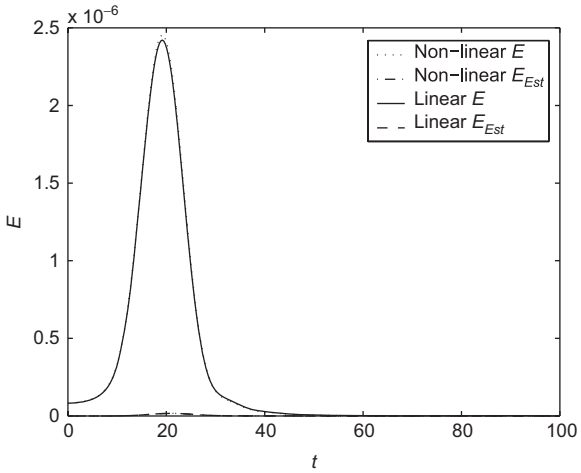

Figure 8. LQG transient energy E vs time t (initial conditions scaled to energy E_{linear}).

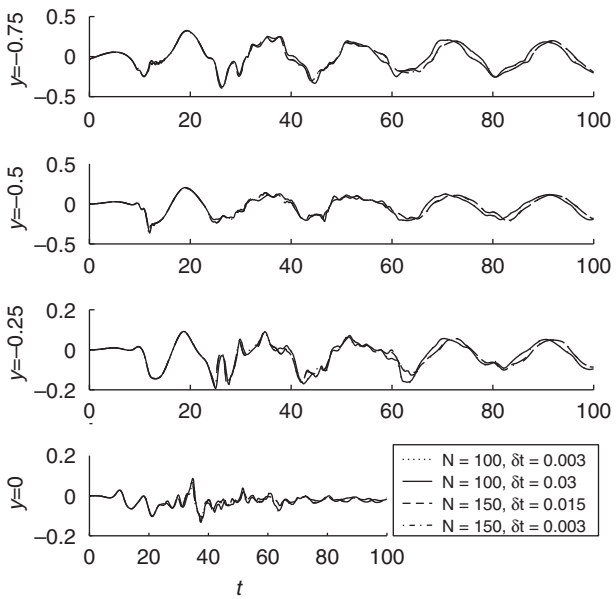

Figure 9. Open-loop u at 4 monitoring points for 2 wall-normal discretizations N and time steps δt.

DOI: 10.1002/fld

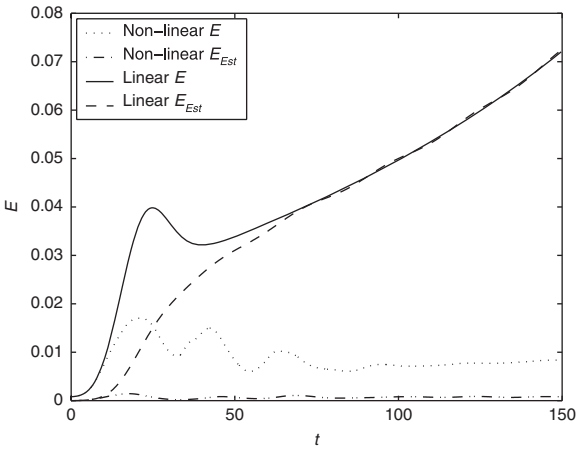

Figure 10. LQE transient energy E vs time t (initial conditions scaled to energy $10^4 E_{\text{linear}}$).

In the streamwise direction the mesh is uniform and has $2^7 = 128$ cells. The results from the two meshes are indistinguishable for approximately 20 time units, while later small differences develop. The results for velocity component v are similar. It can be concluded that reasonable mesh independence can be achieved with 100 cells in the y direction. All subsequent calculations were carried out with a 128×100 mesh. Similarly time step independence justifies a non-dimensional time step $\delta t = 0.03$.

Figure 10 shows the OL transient energy against time, from this larger initial perturbation, for both linear and non-linear simulations. Both simulations agree initially for a short period up to time approximately 10 units. Thereafter the non-linear simulation undergoes an oscillatory transient, and reaches a saturated state, in which the transient energy grows relatively slowly, the value at time 150 being 0.0084 and later at 300 being just 0.0122 (not shown). The CFD results deviate at later times due to the presence of the extra term $(\mathbf{u}\cdot\nabla)\mathbf{u}$ which was discarded from the linear model. The non-linear term couples the equations for different modes, so that energy can be transferred to them. The non-linear analysis allows for harmonics of the wavenumber α since, for example, wavenumber 2α (wavelength π/α) can also fit at a streamwise length of $2\pi/\alpha$. Under these conditions, the mean velocity field is also expected to change and deviate from the original parabolic profile. The number of harmonics that were actually excited was not investigated. However, Jimenez [15] who studied the same non-linear two-dimensional flow reported that the spatial structure of the flow dynamics is rich and needs many Fourier modes for accurate spatial representation; computations are reported with 83 modes. On the other hand, for the linear system there is no mechanism to couple the different modes and the equations decouple by wavenumber.

The same figure also presents the OL estimated transient energy against time. The performance of the linear estimator on the non-linear plant model is poor, achieving a peak energy of only 0.0014 as compared with the plant, which reaches 0.017. The estimator is unable to match the final slow energy growth of the plant.

Figure 11 shows the final ($t = 150$) spanwise vorticity, $\partial v/\partial x - \partial u/\partial y$. This vorticity pattern is in good agreement with the type of the patterns observed in [15]. The author found that the flow reaches an asymptotic state that is dominated by large vortices of alternating sign located near the

DOI: 10.1002/fld

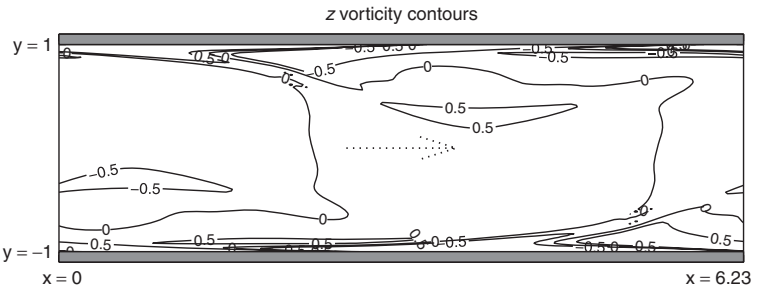

Figure 11. Open-loop final spanwise vorticity contours, from initial conditions $\mathscr{X}_{\text{Worst}}$ scaled to energy, $10^4 E_{C1}$ at $t = 150$.

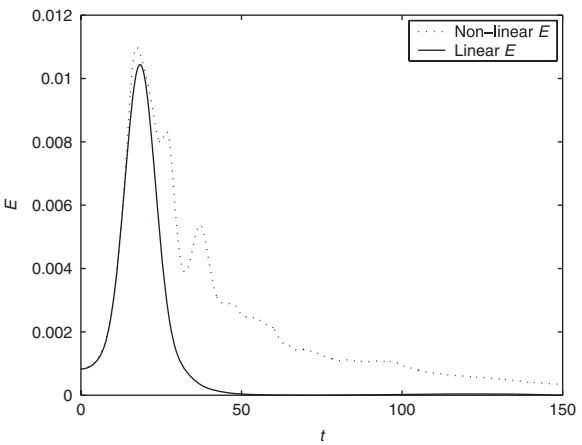

Figure 12. LQR transient energy E vs time t (initial conditions scaled to energy $10^4 E_{\text{linear}}$).

centre of the channel, which induce strong secondary vorticity peaks near the walls. These vortices emanate from the walls periodically, one from the top wall and the other from the bottom wall, as shown in the figure.

The closed-loop LQR transient energy vs time, for both linear and non-linear simulations, is presented in Figure 12. The controller reduces the transient energy, and thus the difference between the linear and non-linear simulation is much reduced, as compared with the OL case. The controller is able to reduce significantly the energy (although it takes significantly longer than in the linear simulation) but cannot entirely relaminarize the flow, at least until 150 time units.

It is reminded that for very small initial disturbances, the energy density evaluated from the state variables (i.e. $E = \mathscr{X}^{\mathrm{T}} 2\mathscr{X}$) agreed very closely to the one evaluated from direct integration of the velocity field over the mesh. For larger perturbations this is not the case. In fact, it was found that the evaluation using the state variables underestimates the peak value of E from direct integration by 77%. This is thought to happen because disturbances at harmonics of the wavenumber α are present in the CFD simulations and energy is transferred to them by non-linear interactions. On

DOI: 10.1002/fld

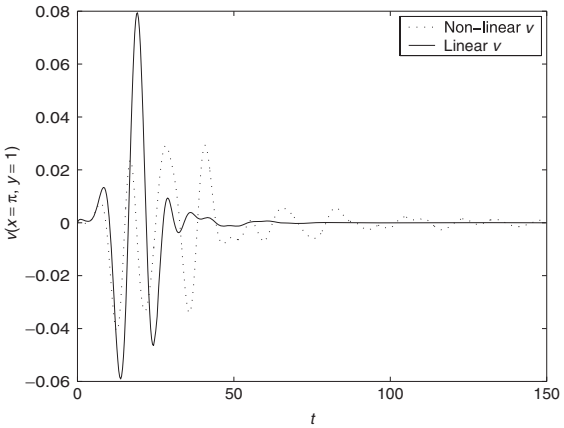

Figure 13. LQR wall transpiration velocity at $x=\pi$ vs time t (initial conditions scaled to energy $10^4 E_{\text{linear}}$).

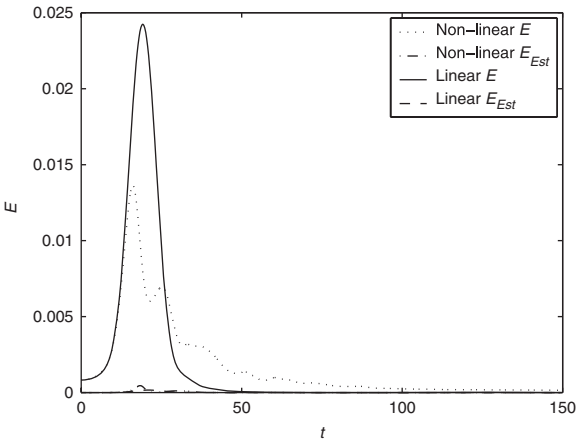

Figure 14. LQG transient energy E vs time t (initial conditions scaled to energy $10^4 E_{\text{linear}}$).

the other hand, the linearly designed controller cannot sense the harmonics and consequently there is large discrepancy between the two results.

Figure 13 displays the upper wall transpiration velocities at location $x=\pi$, the mid point of the domain in x, for the same perturbation. The wall transpiration velocities required in the non-linear simulation are lower than in the linear one, but are required for longer, which is consistent with the transient energy behaviour.

Finally, Figure 14 presents the LQG transient energy vs time. As might be expected, the estimator performs poorly. Surprisingly the estimates it provides are sufficient for the LQR state feedback to stabilize the plant, and at a lower peak transient energy than on the linear plant (0.0136), and only a slightly higher value than the LQR controller achieves on the non-linear plant (0.011).

DOI: 10.1002/fld

6. CONCLUSIONS

The paper has described the synthesis of optimal controllers and estimators for the spectral state-space model of linearized plane Poiseuille flow, which uses a new modified Chebyshev bases in the wall normal direction that automatically satisfies the required boundary conditions and eliminates spurious eigenvalues. An independently derived finite volume Navier–Stokes solver was modified to compute the evolution of perturbations and was employed for open- and closed-loop non-linear simulations of the controllers and estimators. The code was able to accurately reproduce the steady-state transpiration flow field for small transpiration and when supplied with small initial conditions, it accurately reproduced the results of the linear simulations of the open- and closed-loop systems. A mesh and time step sensitivity study was performed to ensure that the non-linear solver produced accurate results from larger initial perturbations, which would trigger significant non-linearity. Simulations from these initial conditions showed initial growth at the same rate as the linear simulations (and thus the relevance of linear control) but the flow reached a saturated state. The state feedback controllers were able to maintain stability and reduced significantly the transient energy; however, the flow did not fully relaminarize, at least until the maximum examined time of 150 units. The non-linear flow energy density was greater than that indicated by the state feedback controller state variables, indicating the probable diversion of energy to harmonics of the considered wavenumber.

REFERENCES

1. Orszag SA. Accurate solution of the Orr–Sommerfeld stability equation. *Journal of Fluid Mechanics* 1971; **50**(4):689–703.
2. Carlson DR, Widnall SE, Peeters MF. A flow-visualization study of transition in plane Poiseuille flow. *Journal of Fluid Mechanics* 1982; **121**:487–505.
3. Butler KM, Farrell BF. Three-dimensional optimal perturbations in viscous shear flow. *Physics of Fluids* 1992; **4**(8):1637–1650.
4. Bewley TR, Liu S. Optimal and robust control and estimation of linear paths to transition. *Journal of Fluid Mechanics* 1998; **365**:305–349.
5. Whidborne JF, McKernan J. On minimizing maximum transient energy growth. *IEEE Transactions on Automatic Control* 2007; **52**(9):1762–1767.
6. Kim J, Bewley TR. A linear systems approach to flow control. *Annual Review of Fluid Mechanics* 2007; **39**:383–417.
7. Zhou K, Doyle JC, Glover G. *Robust and Optimal Control*. Prentice-Hall: Upper Saddle River, NJ, 1996.
8. Skogestad S, Postlethwaite I. *Multivariable Feedback Control* (2nd edn). Wiley: Chichester, England, 2005.
9. Kim J, Lim J. A linear process in wall-bounded turbulent shear flows. *Physics of Fluids* 2000; **12**(8):1885–1888.
10. Baramov L, Tutty OR, Rogers E. *H*-infinity control for non-periodic planar channel flows. *Proceedings of the 40th IEEE Conference on Decision and Control*, Orlando, FL, 4–7 December 2001; 4950–4955.
11. Joshi SS, Speyer JL, Kim J. Finite dimensional optimal control of Poiseuille flow. *Journal of Guidance, Control and Dynamics* 1999; **22**(2):340–348.
12. Zahn JP, Toomre J, Spiegel EA, Gough DO. Non-linear cellular motions in Poiseuille channel flow. *Journal of Fluid Mechanics* 1974; **64**:319–345.
13. Orszag SA, Patera AT. Subcritical transition to turbulence in plane channel flows. *Physical Review Letters* 1980; **45**(12):989–993.
14. Jimenez J. Bifurcations and bursting in two-dimensional Poiseuille flow. *Physics of Fluids* 1987; **30**(12): 3644–3646.
15. Jimenez J. Transition to turbulence in two-dimensional Poiseuille flow. *Journal of Fluid Mechanics* 1990; **218**:265–297.
16. Ehrenstein U, Koch W. Three-dimensional wavelike equilibrium states in plane Poiseuille flow. *Journal of Fluid Mechanics* 1991; **228**:111–148.

DOI: 10.1002/fld

17. Peyret R. *Spectral Methods for Incompressible Viscous Flow* (2nd edn). Applied Mathematical Sciences. Springer: Berlin, 2002.
18. Boyd JP. *Chebyshev and Fourier Spectral Methods* (2nd edn). Dover: Mineola, New York, 2001.
19. Schmid PJ, Henningson DS. *Stability and Transition in Shear Flows*. Applied Mathematical Sciences, vol. 142. Springer: New York, 2001.
20. Gottlieb D, Orszag SA. *Numerical Analysis of Spectral Methods*: *Theory and Applications* (6th edn). Regional Conference Series in Applied Mathematics. SIAM: Philadelphia, PA, 1993.
21. McKernan J. Control of plane Poiseuille flow: a theoretical and computational investigation. *Ph.D. Thesis*, Department of Aerospace Sciences, School of Engineering, Cranfield University, 2006.
22. McKernan J, Papadakis G, Whidborne JF. A linear state-space representation of plane Poiseuille flow for control design: a tutorial. *International Journal of Modelling*, *Identification and Control* 2006; **1**(4):272–280.
23. McKernan J, Whidborne JF, Papadakis G. Linear quadratic control of plane Poiseuille flow—the transient behaviour. *International Journal of Control* 2007; **80**(12):1912–1930.
24. Press WH, Flannery BP, Teukolsky SA, Vetterling WT. *Numerical Recipes*. Cambridge University Press: Cambridge, 1986.

DOI: 10.1002/fld